

Bistable nanomagnet as programmable phase inverter for spin waves

Korbinian Baumgaertl¹ and Dirk Grundler^{1,2, a)}

¹⁾Laboratory of Nanoscale Magnetic Materials and Magnonics, Institute of Materials (IMX),
École Polytechnique Fédérale de Lausanne (EPFL), 1015 Lausanne, Switzerland

²⁾Institute of Microengineering (IMT), École Polytechnique Fédérale de Lausanne (EPFL), 1015 Lausanne,
Switzerland

(Dated: 23 April 2021)

To realize spin wave logic gates programmable phase inverters are essential. We image with phase-resolved Brillouin light scattering microscopy propagating spin waves in a one-dimensional magnonic crystal consisting of dipolarly coupled magnetic nanostripes. We demonstrate phase shifts upon a single nanostripe of opposed magnetization. Using micromagnetic simulations we model our experimental finding in a wide parameter space of bias fields and wave vectors. We find that low-loss phase inversion is achieved, when the internal field of the oppositely magnetized nanostripe is tuned such that the latter supports a resonant standing spin wave mode with odd quantization number at the given frequency. Our results are key for the realization of phase inverters with optimized signal transmission.

Spin wave (SW) computing is promising for future low-power consuming data processing¹⁻³. A common approach for SW logic gates relies on encoding the logic output in the combined amplitude of two (or more) interfering SWs⁴⁻⁹. By inverting the phase of one of the incoming SWs, the output level can be switched from constructive interference with high amplitude (logic '1') to destructive interference with low amplitude (logic '0'). For technological applications an ideal phase inverter should be efficiently gateable, introduce little SW attenuation and operate at the nanoscale. In initial works phase inversion was achieved by exposing SWs to an inhomogeneous magnetic field created by a current carrying wire⁵⁻⁸. To obtain higher efficiency, voltage controlled anisotropy^{9,10} and magnetic defects¹¹⁻¹³ have been explored. In previous works such as Refs.^{12,13} phase shift were detected electrically by propagating spin-wave spectroscopy. Spatially resolved data were not provided. The critical dimension for the phase inversion process and its optimization remained unclear.

In this work we use phase-resolved Brillouin light scattering microscopy (μ BLS)¹⁴⁻¹⁶ to spatially resolve SW wavefronts in a 1D MC with a programmable magnetic defect. We evidence that the previously reported phase shift¹² $\Delta\theta$ occurs locally within the individual magnetic defect. In our experiment, its width amounts to 325 nm much smaller than the SW wavelength λ . So far experimentally observed phase shifts were concomitant with a reduction η in the transmitted SW amplitudes^{12,13}, hindering the performance of the phase inverter. Using micromagnetic simulations we show that the reduction in amplitude can be circumvented by tuning the eigenfrequency of the magnetic defect such that resonant coupling is achieved. Our findings are promising for the realization of a low-loss nanoscale

phase inverter in magnonics.

Figure 1(a) shows a scanning electron microscopy (SEM) image of the investigated sample. The 1D MC consisted of dipolarly coupled $\text{Co}_{20}\text{Fe}_{60}\text{B}_{20}$ nanostripes arranged periodically with a period $p = 400$ nm. Nanostripes were 325 nm wide, (19 ± 2) nm thick and 80 μm long. A single stripe in the center of the MC was elongated on both sides by 8 μm to increase its coercivity. By tuning the magnetic history, we magnetized the short stripes in $+y$ -direction, while the prolonged stripe was magnetized in $-y$ -direction (Fig. 1(b)). In this state, the prolonged stripe is magnetized in opposite direction compared to the rest of the MC, i.e., the short stripes, and we refer to it as *magnetic defect*. On top of the MC two coplanar waveguides (CPWs) with signal and ground line widths of 0.8 μm were prepared out of 5 nm thick Ti and 110 nm Au. For phase-resolved spin wave transmission experiments based on all-electrical spectroscopy both CPWs were used. Spectra were reported in Ref.¹² (sample MC1). In the presented study we go beyond the earlier studies¹¹⁻¹³ and exploit focused laser light to investigate microscopic aspects of the phase shifting process with high spatial resolution. We excited SWs by applying a microwave current at CPW1 and used μ BLS for detection. Figure 1(c) shows an optical image of MC1 taken with the μ BLS camera. We focused a laser with a wavelength of 473 nm and 1 mW power to a spot with a diameter of about 350 nm onto the sample surface. The laser spot was scanned in $+x$ -direction in 100 nm steps, while SW intensity and phase were measured (see yellow scan path in Fig. 1(c)). A magnetic field $\mu_0 H_B$ was applied in $+y$ -direction, corresponding to the magnetization direction of the short stripes.

The 1D MC with magnetic defect was investigated for several $\mu_0 H_B$. Then the prolonged stripe was magnetized in $+y$ -direction and measurements were performed on the defect-free MC1 using identical instrument settings.

^{a)}Electronic mail: dirk.grundler@epfl.ch

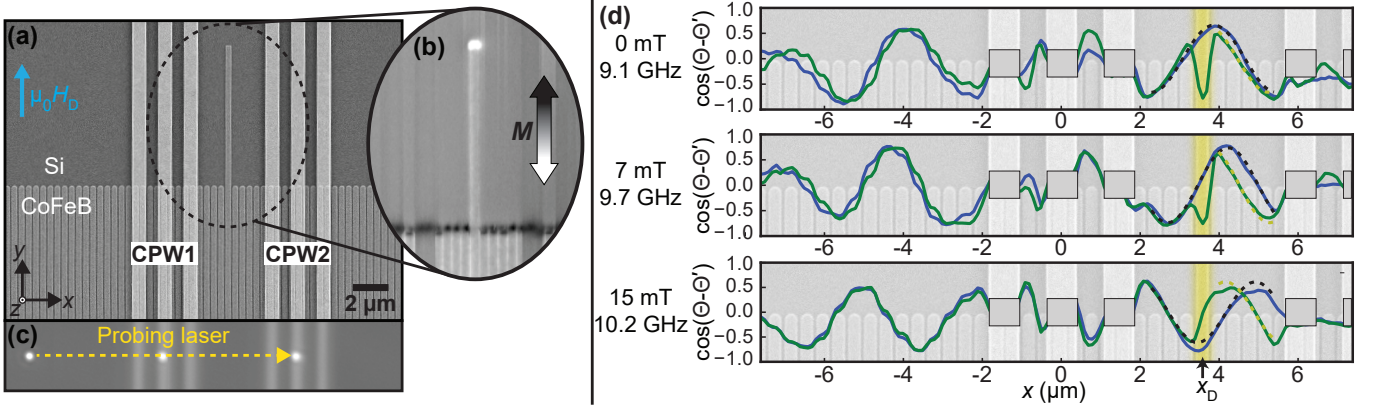


FIG. 1. (a) SEM and (b) magnetic force microscopy image of the central region of MC1. The elongated nanostripe was intentionally magnetized in $-y$ -direction opposed to the magnetization of the short stripes in order to form a magnetic defect. (c) Optical image of MC1 as seen in the BLS microscope. The probing laser spot was scanned along the yellow dashed line, while SW intensity and phase signal was recorded. Microwave excitation was applied to CPW1. (d) Phase signal measured with (green lines) and without (blue lines) magnetic defect for different H_B (rows). The position x_D of the magnetic defect is highlighted.

The microwave frequency f_{ex} used for excitation was adapted for each H_B in order to excite a SW with $k_1 = 2\pi/\lambda = 2.0 \text{ rad } \mu\text{m}^{-1}$ ¹². Thereby we excite a SW with $\lambda = 3.1 \text{ } \mu\text{m}$ which is more than 9 times larger than the width of the magnetic defect. We use micromagnetic simulations with MuMax3¹⁷ to explore $\Delta\Theta$ and η for a wide range of bias fields and wave vectors. We simulated a slice of MC1 in the x - z -plane, while in y -direction the periodic boundary condition (PBC) approach¹⁸ with 1024 repetitions in $+y$ and $-y$ -direction was applied, assuming a constant magnetization of nanostripes along their lengths. We used $\mu_0 M_s = 1.8 \text{ T}$ as saturation magnetization¹², $\alpha = 0.006$ as Gilbert damping¹⁹, $A_{\text{ex}} = 20 \text{ pJ m}^{-1}$ as exchange constant²⁰ and a grid size of $2 \text{ nm} \times 20 \text{ nm} \times 2 \text{ nm}$ ($\Delta x, \Delta y, \Delta z$). For band structure simulations a chain of 40 stripes and for SW propagation a chain of 164 stripes was considered.

Following Refs.^{21,22} we simulated band structures by exciting the MC with a spatially and temporally varying magnetic field (given by sinc functions) and subsequent computation of the Fourier amplitudes of the dynamic magnetization components $m_x(x, t)$ and $m_y(x, t)$. We obtained a good agreement with the measured band structure of MC1¹², when the simulated film thickness was reduced to $d = 10 \text{ nm}$ (supplement Fig. S1). The discrepancy with the nominal value of d might be due to film roughness in the real sample, which reduced the surface pinning²³ and was not considered in the simulations.

For simulating SW transmission through a magnetic defect, SWs were excited locally at $x = 0 \text{ } \mu\text{m}$ by a sinusoidal h_{rf} exploring different frequencies f_{ex} at different H_B . An individual stripe at $x_D = 6 \text{ } \mu\text{m}$ was magnetized in $-y$ -direction. The other stripes were magnetized in $+y$ -direction. We analyzed amplitudes and phases of $m_x(x, t)$ and $m_z(x, t)$ after the simulations

had run for $t' = 10 \text{ ns}$ and propagating SWs had reached a steady state. To avoid back-reflection, an absorbing boundary condition following Ref.²⁴ was applied at the outer edges of the MC.

Figure 1(d) displays the SW phase signal measured for MC1 with magnetic defect (green lines) and without (blue lines) at specific $\mu_0 H_B$. Phase-resolved μBLS allowed us to measure $\cos(\Theta(x) - \Theta')$, where $\Theta(x)$ is the SW phase at a position x and Θ' is a reference phase²⁵. Θ' is constant for a given frequency f_{ex} . For all $\mu_0 H_B$, we observed sinusoidal waves with a wavelength $\lambda \simeq 3.1 \text{ } \mu\text{m}$. In the defect-free state (all stripes magnetized in one direction), the sinusoidal wave profile was unperturbed at the position x_D of the prolonged stripe. We assume that due to the large aspect ratio of the investigated nanostripes, the demagnetization factor in y -direction was already close to zero for all nanostripes²⁶ and the additional prolongation had little impact on the nanostripe's demagnetization field. When the prolonged stripe was oppositely magnetized (magnetic defect state) the phase was clearly modified at $x = x_D$. For $\mu_0 H_B = 0 \text{ mT}$ (top row in Fig. 1(d)) a localized phase jump (dip) was observed at x_D . For $x > x_D$, the phase profiles with and without defect were still in good agreement. We attribute the localized phase jump at x_D to an in-plane dynamic coupling of the defect's magnetization to its neighboring stripes, as suggested in Huber *et al.*²⁷. Due to magnetic gyrotropy, the sense of spin-precessional motion in the defect is opposite to the rest of the MC. Consequently, the in-phase coupling results in a π phase jump of the dynamic out-of-plane magnetization component, which is detected by μBLS .

For increasing $\mu_0 H_B$ (second and third row in Fig. 1(d)), the phase profiles with and without defect were significantly displaced relative to one another for $x > x_D$. The displacements indicate phase shifts of

SWs. Strikingly, the relative displacements were pronounced directly at the defect, i.e. the phase shifts were established on the length scale of the individual stripe of width $w = 325$ nm. We quantify phase shifts $\Delta\Theta$ by fitting cosine functions $\cos(\Theta(x) - \Theta')$ for SWs which passed the defect (yellow) and SWs in the defect-free state (black dashed lines in Fig. 1(d)). The blue line in Fig. 2 displays the extracted $\Delta\Theta$ as a function of $\mu_0 H_B$. In good agreement with Ref. ¹², we find a monotonous increase of $\Delta\Theta$ with $\mu_0 H_B$ reaching a phase shift close to $\pi/2$ at 15 mT. The experiments of Fig. 1(d) reveal the nanoscale nature of the phase shifting mechanism. The phase shift was concomitant with a reduction in the amplitude of transmitted SWs (details in Supplement Fig. S2). The green line in Fig. 2 displays the ratio η of measured SW amplitudes with and without defect for $x > x_D$. At 15 mT the defect reduced the SW amplitude by a factor of 2.

In Fig. 3 we present micromagnetic simulations displaying results in the vicinity of the defect for $\mu_0 H_B = 0$ mT and a SW with $k_x \approx 2$ rad μm^{-1} . The first row in Fig. 3 displays a snapshot of $m_x(x, t')$ and $m_z(x, t')$ at t' . Due to the ellipticity of the magnetization precession the amplitude of m_z was small compared to m_x and multiplied by a factor of 10 for better visibility. We recorded m_x and m_z for $t \geq t'$ in 10 ps steps during a time span of 2 ns and computed the FFT amplitude (Amp) and phase (Θ) at the driving frequency f_{ex} . Amp(m_x) and Amp(m_z) are displayed in the second row of Fig. 3. The SWs decayed exponentially with a decay length $\delta = 3.15$ μm , which was in good agreement with $\delta = 2.9 \pm 0.2$ μm observed in the experiment (see Fig. S2). At the defect, no significant change in amplitude was visible for $\mu_0 H_B = 0$ mT. In the third row, we plot $\cos(\Theta - \Theta')$ for $\Theta(m_x)$ and $\Theta(m_z)$ extracted at the center of each stripe. $\Theta(m_x)$ followed a sinusoidal wave with $\lambda \sim 3$ μm (blue dashed line in Fig. 3) without deviation at the defect. For $\Theta(m_z)$ however a local phase jump of π is apparent at the defect (orange dashed line in Fig. 3), which agrees well with the measurement observation on MC1 for $\mu_0 H_B = 0$ mT (cf. first row in Fig. 1(d)).

For a quantitative analysis of amplitude and phase

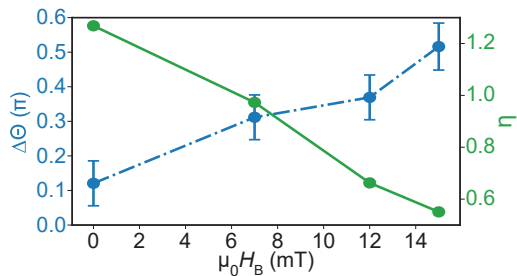


FIG. 2. Measured phase shift $\Delta\Theta$ (blue line) and attenuation ratio η (green) for SWs at $x > x_D$ with magnetic defect compared to SWs without defect.

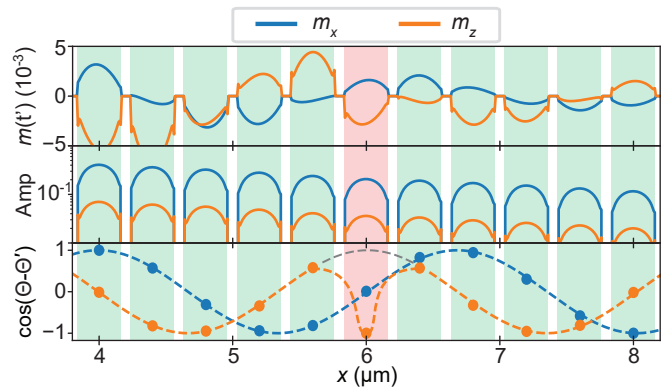


FIG. 3. Simulated m_x and m_z for a propagating SW excited at $x = 0$ μm with $k_x \approx 2$ rad μm^{-1} shown for $\mu_0 H_B = 0$ mT. The stripe at $x_D = 6$ μm (marked in red) was oppositely magnetized. The first row shows a snapshot of m_x and m_z at $t' = 10$ ns. The second and third row depicts the precessional amplitudes and cosine of the phase. At the defect a π phase jump of the phase of m_z is observed.

changes introduced by the defect, we repeated simulations for the defect-free state as a reference. We computed η as the ratio of Amp(m_x) values with and without defect. Further we computed the magnitude of the phase shift $|\Delta\Theta|$ based on the difference of $\Theta(m_x)$ with and without defect. Both η and $|\Delta\Theta|$ were evaluated in the region $x = 8$ to 12 μm and then averaged. Bias fields from 0 to 44 mT were simulated in 4 mT steps. We note that in the simulations the defect was not switched up to 44 mT, while in our experiments the defect switched at 23 mT. Switching fields in real stripes with rough edges have already been reported to be smaller compared to stripes with ideal edges in simulations²⁸. For each H_B , we computed the dispersion relation and extracted frequencies of the first miniband at $k_x = k_1 = 2$ rad μm^{-1} (as used in the experiment) and $k_x = 4$ rad μm^{-1} (in the middle of the first Brillouin zone of the MC). Then SW propagation was simulated for the extracted frequencies. In this manner, we evaluated η and $|\Delta\Theta|$ as a function of H_B without significantly varying the wave vector (Fig. 4(a) and (b)). For $k_x \approx 2$ rad μm^{-1} we observe a decrease in transmission with H_B until $\mu_0 H_B = 24$ mT, where η reaches a minimum value of 0.06. In the same field regime we extract an approximately linear increase of $|\Delta\Theta|$ from 0 to 0.88π , which is in good qualitative agreement with our experimental data (Fig. 2).

Strikingly, above 24 mT the simulated transmission coefficient η started to increase with H_B . Concomitantly $|\Delta\Theta|$ further increased. For $k_x = 2$ rad μm^{-1} we found $\eta = 0.65$ at 40 mT. $|\Delta\Theta|$ peaked at 36 mT, amounting to 0.95π . For $k_x \approx 4$ rad μm^{-1} , the maximum in $|\Delta\Theta|$ coincided with the local maximum in η for $\mu_0 H_B = 36$ mT. We found $|\Delta\Theta| = 0.92\pi$ and an appreciable transmission with $\eta = 0.73$, allowing for low-loss phase inversion. In the following we discuss the origin of the large η

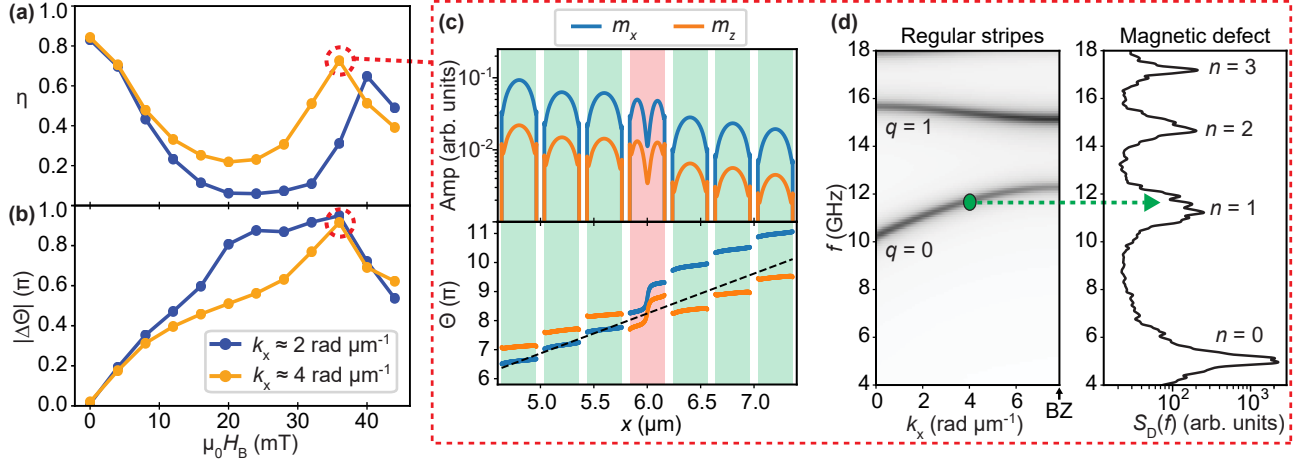


FIG. 4. (a) Simulated amplitude ratio η and (b) phase shift $|\Delta\Theta|$ as function of an applied bias field. For SWs with $k_x \approx 4 \text{ rad } \mu\text{m}^{-1}$ a large η and close to π phase shift was achieved at 36 mT (marked by red circle). In (c) we display the respective amplitude and phase evolution. The dynamic magnetization profile at the defect indicates a laterally standing mode with quantization number $n = 1$. (d) Dispersion relation of the 1D MC and the power spectral density $S_D(f)$ of thermally excited magnons at the defect simulated for $\mu_0 H_B = 36 \text{ mT}$, respectively. The frequency of SWs with $4 \text{ rad } \mu\text{m}^{-1}$ in the first miniband ($q = 0$) of the MC matches with the frequency of the second spin wave resonance $n = 1$ of the defect.

for high H_B . Figure 4(c) shows Amp and Θ for SWs with $k_x \approx 4 \text{ rad } \mu\text{m}^{-1}$ excited at $f_{\text{ex}} = 11.73 \text{ GHz}$ and $\mu_0 H_B = 36 \text{ mT}$. The plotted Θ has been unwrapped and the slope (black dashed line) represents $\Theta - \Theta' = k_x x$. The phase evolution of stripes neighboring the defect behaves regularly. The phase shift occurs right at the center of the defect, where Θ abruptly shifts by about π . At the same position, a node in the SW amplitude is observed. The dynamic magnetization profile along the width of the defect agrees well with a standing wave with quantization number $n = 1$ ²⁹. To identify the eigenfrequencies of the magnetic defect, we simulated with MuMax3 thermally excited magnons at a finite temperature $T = 300 \text{ K}$ ³⁰. The simulation was run over an extended time period of 100 ns and then the power spectral density $S_D(f)$ of $m_x(t)$ at the position of the defect was computed. Allowed SW eigenfrequencies are apparent as peaks in $S_D(f)$ ³⁰⁻³². By considering thermal magnons we are not limited to SW modes compatible with the symmetry of an exciting h_{rf} .

Figure 4(d) compares the band structure of the 1D MC and $S_D(f)$ of the magnetic defect for $\mu_0 H_B = 36 \text{ mT}$. Here the frequency of SWs with $k_x = 4 \text{ rad } \mu\text{m}^{-1}$ in the first miniband ($q = 0$) matches well with the frequency of the second allowed state ($n = 1$) observed in $S_D(f)$. In the contrary for 24 mT, where the transmission was low, the relevant f_{ex} was between the $n = 0$ and $n = 1$ peaks of $S_D(f)$ (Supplement Fig. S3), i.e. inside a forbidden frequency gap. Our finding suggests that high transmission is obtained when one of the eigenfrequencies of the defect is resonantly tuned to f_{ex} . We speculate that for larger H_B not considered in the simulation, further maxima in η are achieved every time the frequency of SWs excited in a miniband q of the regular magnetized stripes overlaps with a higher

eigenfrequency state $n = q + i$ (with $i \in \mathbb{N}$ and $i \geq 2$) at the defect. Based on the dynamic magnetization profiles know for laterally standing waves in a nanostripe^{29,33,34}, we anticipate a phase shift of $\sim \pi$ in case $n - q$ is odd and $\sim 0\pi$ in case $n - q$ is even.

To conclude, via phase-resolved μBLS we measured the phase evolution of propagating SWs in a 1D MC consisting of dipolarly-coupled nanostripes. When a single nanostripe was magnetized in opposing direction, a local phase jump of the out-of-plane dynamic component was detected. For $\mu_0 H_B > 0 \text{ mT}$, phase shifts occurred on the length scale of 325 nm much smaller than λ , and were concomitant with a reduction in transmission amplitude. Using micromagnetic simulations we found however an increase in transmission, once the bias field was sufficient to align the magnon miniband with the eigenfrequency of the second laterally quantized mode in the defect. Due to the resonant coupling of the defect, a high transmission and a phase shift of close to π were achieved, allowing for a low-loss phase inverter. For future experimental studies, it will be relevant to either increase the switching field (e.g. by using a material with an appropriate magnetocrystalline anisotropy) or to reduce the frequency spacing of the minibands. The latter could be realized for 1D MCs prepared from Yttrium iron garnet. Our results pave the way for efficient and low-loss phase inverters in nanomagnonics.

Supplementary Material

See supplementary material for a comparison of the simulated and experimental dispersion relation, SW intensities measured with μBLS , and the simulated dispersion relation and $S_D(f)$ at $\mu_0 H_B = 24 \text{ mT}$.

Acknowledgment

We thank for funding by SNSF via grant 163016. We thank F. Stellacci, E. Athanasopoulou and S. Watanabe for support concerning MFM.

Data Availability

The data that support the findings of this study are openly available in Zenodo at <http://doi.org/10.5281/zenodo.4680409>.

- ¹A. V. Chumak, V. I. Vasyuchka, A. A. Serga, and B. Hillebrands, *Nat. Phys.* **11**, 453 (2015), review.
- ²G. Csaba, Á. Papp, and W. Porod, *Phys. Lett. A* **381**, 1471 (2017).
- ³A. Mahmoud, F. Ciubotaru, F. Vanderveken, A. V. Chumak, S. Hamdioui, C. Adelmann, and S. Cotofana, *Journal of Applied Physics* **128**, 161101 (2020).
- ⁴R. Hertel, W. Wulfhekel, and J. Kirschner, *Phys. Rev. Lett.* **93**, 257202 (2004).
- ⁵M. P. Kostylev, A. A. Serga, T. Schneider, B. Leven, and B. Hillebrands, *Appl. Phys. Lett.* **87**, 153501 (2005).
- ⁶K.-S. Lee and S.-K. Kim, *Journal of Applied Physics* **104**, 053909 (2008).
- ⁷T. Schneider, A. A. Serga, B. Leven, B. Hillebrands, R. L. Stamps, and M. P. Kostylev, *Appl. Phys. Lett.* **92**, 022505 (2008).
- ⁸O. Rousseau, B. Rana, R. Anami, M. Yamada, K. Miura, S. Ogawa, and Y. Otani, *Scientific reports* **5**, 9873 (2015).
- ⁹B. Rana and Y. Otani, *Phys. Rev. Applied* **9**, 014033 (2018).
- ¹⁰B. Rana and Y. Otani, *Communications Physics* **2** (2019), [10.1038/s42005-019-0189-6](https://doi.org/10.1038/s42005-019-0189-6).
- ¹¹S. Louis, I. Lisenkov, S. Nikitov, V. Tyberkevych, and A. Slavin, *AIP Advances* **6**, 065103 (2016).
- ¹²K. Baumgaertl, S. Watanabe, and D. Grundler, *Appl. Phys. Lett.* **112**, 142405 (2018).
- ¹³O. V. Dobrovolskiy, R. Sachser, S. A. Bunyaev, D. Navas, V. M. Bevez, M. Zelent, W. Śmigaj, J. Rychły, M. Krawczyk, R. V. Vovk, M. Huth, and G. N. Kakazei, *ACS Applied Materials & Interfaces* **11**, 17654 (2019).
- ¹⁴A. A. Serga, T. Schneider, B. Hillebrands, S. O. Demokritov, and M. P. Kostylev, *Appl. Phys. Lett.* **89**, 063506 (2006).
- ¹⁵V. E. Demidov and S. O. Demokritov, *IEEE Transactions on Magnetics* **51**, 1 (2015).
- ¹⁶T. Sebastian, K. Schultheiss, B. Obry, B. Hillebrands, and H. Schultheiss, *Front. Phys.* **3**, 35 (2015).
- ¹⁷A. Vansteenkiste, J. Leliaert, M. Dvornik, M. Helsen, F. Garcia-Sanchez, and B. Van Waeyenberge, *AIP Adv.* **4**, 107133 (2014).
- ¹⁸H. Fangohr, G. Bordignon, M. Franchin, A. Knittel, P. A. J. de Groot, and T. Fischbacher, *J. Appl. Phys.* **105**, 07D529 (2009).
- ¹⁹C. Bilzer, T. Devolder, J.-V. Kim, G. Counil, C. Chappert, S. Cardoso, and P. P. Freitas, *J. Appl. Phys.* **100**, 053903 (2006).
- ²⁰T. Devolder, J.-V. Kim, L. Nistor, R. Sousa, B. Rodmacq, and B. Diény, *J. Appl. Phys.* **120**, 183902 (2016).
- ²¹M. Dvornik, A. N. Kuchko, and V. V. Kruglyak, *J. Appl. Phys.* **109**, 07D350 (2011).
- ²²D. Kumar and A. O. Adeyeye, *J. Phys. D: Appl. Phys.* **50**, 343001 (2017).
- ²³D. Mercier and J.-C. S. Lévy, *J. Magn. Magn. Mater.* **163**, 207 (1996).
- ²⁴G. Venkat, H. Fangohr, and A. Prabhakar, *J. Magn. Magn. Mater.* **450**, 34 (2018), perspectives on magnon spintronics.
- ²⁵F. Fohr, A. A. Serga, T. Schneider, J. Hamrle, and B. Hillebrands, *Rev. Sci. Instrum.* **80**, 043903 (2009).
- ²⁶A. Aharoni, *Journal of Applied Physics* **83**, 3432 (1998), <https://doi.org/10.1063/1.367113>.
- ²⁷R. Huber, T. Schwarze, and D. Grundler, *Phys. Rev. B* **88**, 100405 (2013).
- ²⁸J. Topp, G. Duerr, K. Thurner, and D. Grundler, *Pure Appl. Chem.* **83**, 1989 (2011).
- ²⁹K. Y. Guslienko, S. O. Demokritov, B. Hillebrands, and A. N. Slavin, *Phys. Rev. B* **66**, 132402 (2002).
- ³⁰J. Leliaert, J. Mulkers, J. De Clercq, A. Coene, M. Dvornik, and B. Van Waeyenberge, *AIP Adv.* **7**, 125010 (2017).
- ³¹N. Smith, *J. Appl. Phys.* **90**, 5768 (2001).
- ³²J. Yoon, C. You, Y. Jo, S. Park, and M. Jung, *J. Korean Phys. Soc.* **57**, 1594 (2010).
- ³³C. Mathieu, J. Jorzick, A. Frank, S. O. Demokritov, A. N. Slavin, B. Hillebrands, B. Bartenlian, C. Chappert, D. Decanini, F. Rousseaux, and E. Cambri, *Phys. Rev. Lett.* **81**, 3968 (1998).
- ³⁴G. Gubbiotti, S. Tacchi, G. Carlotti, P. Vavassori, N. Singh, S. Goolaup, A. O. Adeyeye, A. Stashkevich, and M. Kostylev, *Phys. Rev. B* **72**, 224413 (2005).